2021

Comprehensive Modeling of a Chemical Looping Heat Pump with a Reverse Fuel Cell

Junyoung Kim
Purdue University, junyoungkim@purdue.edu

Nelson A. James
U.S. Department of Energy

James E. Braun

Eckhard A. Groll
Purdue University

Davide Ziviani
Purdue University

Comprehensive Modeling of a Chemical Looping Heat Pump with a Reverse Fuel Cell

Junyoung KIM [1], James E. BRAUN [1]*, Eckhard A. GROLL[1]*, Davide ZIVIANI [1]*

[1] Ray W. Herrick Laboratories, School of Mechanical Engineering, Purdue University
West Lafayette, 47907-2099, USA
junyoungkim@purdue.edu; jbraun@purdue.edu; groll@purdue.edu; dziviani@purdue.edu

* Corresponding Author

ABSTRACT

HVAC, refrigeration, and water heating accounted for approximately 22 quads of primary energy consumed in the United States in 2018, according to US EIA. Most of HVAC&R industry still relies on vapor compression and heat-driven technologies. The development of highly efficient technologies that would significantly improve both COP and annual energy savings is an open challenge for the new decade. Among the novel technologies, the Chemical Looping Heat Pump (CLHP) combined with a reverse fuel cell has been modeled with estimates of a COP increase of over 20% relative to a conventional vapor compression (VC) cycle. However, limitations of simplified modeling efforts necessitate the development of a comprehensive mechanistic model to predict several physical phenomena for varying operating conditions and more accurately estimate performance.

In this work, a charge-sensitive mechanistic modeling approach is utilized to predict the performance of the CLHP system. A thermodynamic model is coupled with a discretized fuel cell model to estimate the energy savings potential. A moving boundary model is adopted to assess the steady-state heat transfer rate in the heat exchanger. Sensitivity analyses are used to identify the system behaviors and performance.

Keywords: non-vapor compression, CLHP, fuel cell, mechanistic model, energy savings

1. INTRODUCTION

The buildings' sector has played an outsized role in the US energy consumption. It is estimated that more than a 40% of the US primary energy use and 75% of the US electricity are associated with buildings. Among this, nearly half of the energy usage is due to space heating, cooling, and refrigeration (US EIA, 2019). Many of the end uses heavily rely on vapor-compression technologies for serving the needs of heating and cooling demands. However, conventional refrigerants used in vapor-compression systems contribute to detrimental environmental impacts (an emission of 700 $MMTCO_2$) due to direct and indirect emissions into the atmosphere (Goetzler et al., 2016). As a result, several government entities have addressed a hydrofluorocarbon refrigerants (HFCs) phasedown proposal, which targets an 85 % reduction by 2035 (US DOE BTO, 2016; European Commission, 2013).

To meet these goals, several research institutes have proposed alternatives to vapor-compression technologies. For example, the US government addressed a combination of short- and long-term approaches for developing the next generation of HVAC&R as indicated in Figure 1(a). In this report, cost-effective non-vapor compression technologies have been proposed as a long-term direction. In addition, Goetzler et al. (2014) and Fil et al. (2021) quantitatively benchmarked alternative heat pumping technologies to baseline vapor-compression technology and one of examples is shown in Figure 1(b). Some of these alternatives provide additional non-energy benefits including improved air quality, improved reliability, and the use of environmentally friendly working fluids.

Among the novel technologies, the chemical looping heat pump (CLHP) has been proposed as a promising and valuable alternative for high efficiency heat pumping (James et al., 2019; Kim et al., 2020). The concept utilizes redox reactions in an electrochemical cell to which the working fluid properties are alternated between more and less volatile states at a given coulombic input. By doing so, a compressor can be replaced with a pump, requiring less work input for driving heat pumping effects. In previous research efforts, it has been estimated that the CLHP system could increase the system COP by more than 20% as compared to a conventional vapor compression system (James et al., 2019).

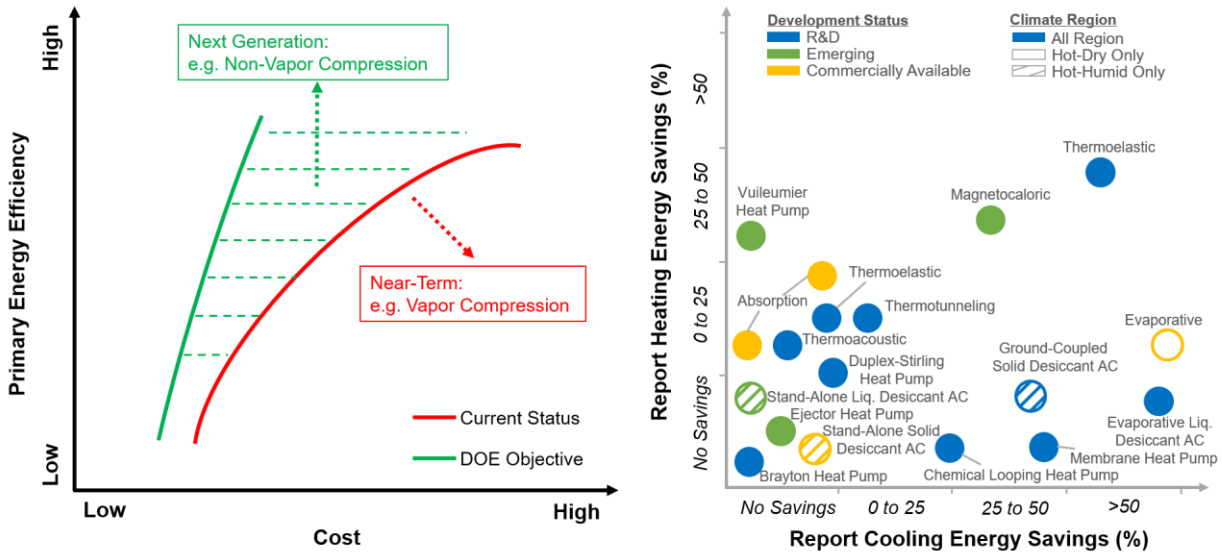

(a) **(b)**

Figure 1: (a) The US DOE BTO strategies for a development of a next generation HVAC&R (modified from Goetzler et al., (2016)) (b) Potential energy savings and developmental status of 18 alternative heat pumps (reproduced from Goetzler et al., (2014))

In this work, a charge-sensitive mechanistic model is developed to predict the performance of the CLHP system by modifying the open-source framework ACHP (Bell, 2015). The work is an extension of a previous study published from Kim et al. (2020) and James (2019), where a 2D-discretized cell model was integrated with a simplified thermodynamic model to assess the system performance. Unlike the previous work, a moving boundary model is adopted to assess the steady-state heat transfer rate and pressure drops in the heat exchanger and line sets. In addition, charge inventory calculations are added. The model was developed to mechanistically estimate the system pressures and temperatures of the proposed system for given geometries and operating conditions. Sensitivity analyses are used to identify the system behaviors and performance.

2. CHEMICAL LOOPING HEAT PUMP

2.1 System Description

The CLHP is composed of a portion of a conventional vapor compression cycle integrated with a reverse fuel cell. Among various fuel cell types, a proton exchange membrane fuel cell (PEMFC) is selected as a reactor due to operating conditions that are similar to those of heat pumps (James et al., 2019; Kim et al., 2020). The important mechanism is dehydrogenation and hydrogenation reactions, where the saturation pressures of the working fluids are changed, which can in turn lead to the fluid being in the liquid phase after coming out of the evaporator. From previous research work, ketones have been identified as possible working fluid candidates (James et al., 2019).

A general working principle of the CLHP system is shown in Figure 2. The liquid fluid (*e.g.*, IPA) at state 1 is pressurized by a pump, resulting in the working fluid exiting at a high pressure. Then, the high-pressure liquid passes through the reverse fuel cell, where oxidation (dehydrogenation) at the anode changes the fluid into a more volatile fluid (*e.g.*, acetone) at state 2. A regenerator is utilized to pre-cool the fluid before entering the expansion valve at state 2-b. The overall processes between state 2-b and state 4-b are quite similar to those of a conventional vapor compression cycle. Lastly, the reduction reaction (hydrogenation) at the cathode transforms the gaseous fluid (e.g., acetone) back into the liquid fluid (e.g., IPA) before flowing through the pump (Kim et al., 2020).

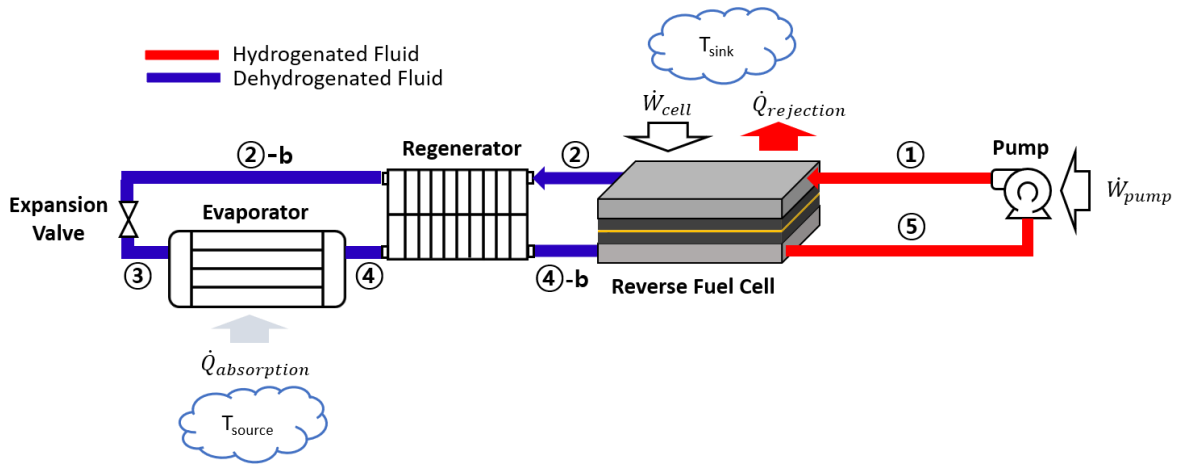

Figure 2: Schematic of Chemical Looping Heat Pump

2.1 System Modeling

A charge-sensitive mechanistic modeling has been widely used in vapor compression and waste heat recovery technologies (Bahman et al. (2018); Ziviani et al. (2016)). This approach allows estimates of realistic system pressures and temperatures by an iteration process of pre-defined independent variables for given geometries, surroundings, and working fluid charge levels. Based on these considerations, the CLHP model has been upgraded based on previously developed thermodynamic models and sub-component models from the ACHP open-source code. Detailed mathematical equations can be obtained in Kim et al. (2020) and Bell (2015). In this work, special attention is paid to the solution method for achieving the mechanistic model.

The logic behind the solution algorithm is summarized in the left plot of Figure 3. At first, the solution process requires proper initial guess values to initiate an iterative multi-dimensional solver. To achieve this, a simplified thermodynamic model published in James et al. (2019) is employed as a guess-generator model (pre-conditioner model). Assuming complete chemical reactions, this model finds the system pressures and temperatures using Broyden's method (Broyden, 1965) until satisfying a system energy balance criterion, and then feeds these output values to the main cycle solver. However, future work is necessary to consider incomplete chemical reactions in the pre-conditioner model in order to establish better initial guesses.

To obtain the solution, iterative processes are used with the independent parameters passing through the component-level models. The reverse fuel cell model, in particular, utilizes these input parameters for an iteration to decide the required cell power. Two independent parameters, a cell temperature (T_{cell}) and an extent of reaction in the cell ($\Delta\xi$), are defined that determine the system pressures and temperatures. These variables are iteratively adjusted within the main cycle solver until a pre-defined residual vector satisfies a convergence criterion. To avoid unexpected divergence during calculations, a bounded scalar optimization solver (Powell, 1964) is adopted to achieve a robustness solution. As indicated in the right plot of Figure 3, two scalar components of the residual vector are defined with an L-infinity norm that is used for a convergence evaluation that ensures a system energy balance.

2.2 Pump Modeling

By assuming that the fluid behaves as an incompressible liquid, the pump power can be estimated at given mass flow rates as indicated in Eq. (1), where an isentropic efficiency accounts for the irreversibilities during the process.

$$\dot{W}_{pump} = \frac{\dot{m}v(P_{high} - P_{low})}{\eta_{pump}} \tag{1}$$

Here, η_{pump} is a constant pump efficiency, υ refers to the specific volume, and P_{high} and P_{low} correspond to the system pressures. It is important to note that mass flow rates on the order of μg/s ~ mg/s are of interest for performance assessments and control purposes in this study. This scale of flow rate is chosen based on a test-stand that was built and the state-of-the-art literature (McKay et al., 2019; Poletayev et al., 2018).

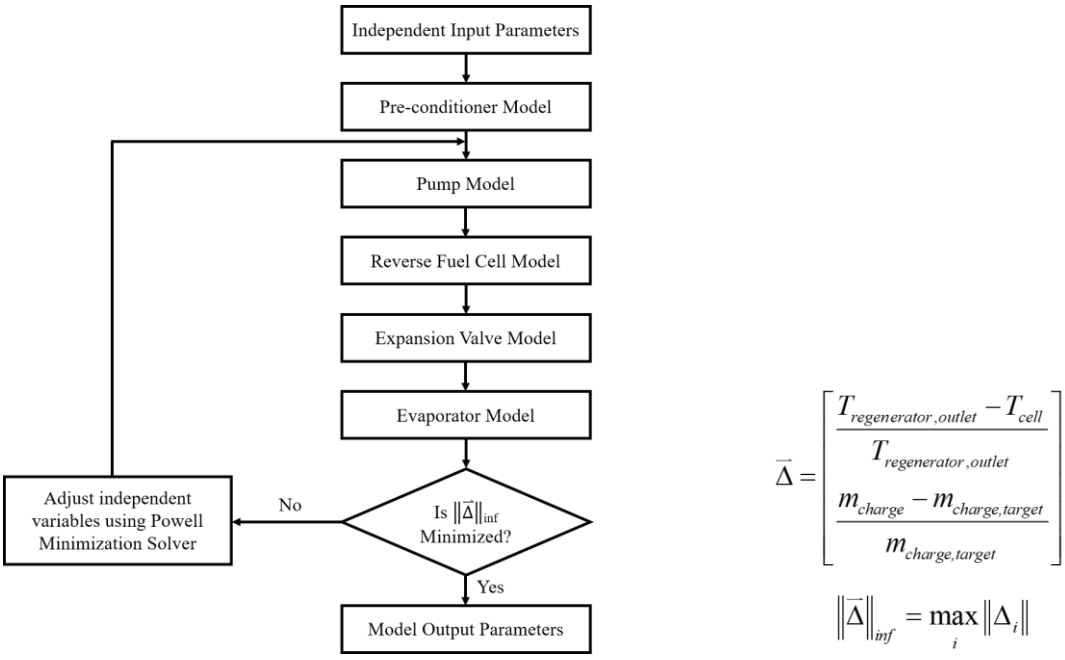

Figure 3: Cycle Model Algorithm (Left) and Residual Vector and L-infinity Norm (Right)

2.3 Reverse Fuel Cell Modeling

A 2D-discretized cell model has been developed by the authors to perform an accurate estimation of cell performance. The complete equations and fundamentals can be found in Kim et al. (2020) and James et al. (2019). In this paper, the key concepts of the detailed cell modeling are described. As seen in Figure 4, the cell is first divided into 9 domains in the y-direction, and then discretized into 25 segments along the x-direction based on a mesh convergence study. Along with the y-direction, the different transport terms are summarized in Table 1. The properties of the working fluid are changing in the x-direction. By assuming that the outer surface of the cell is well insulated, a cooling rate from the cooling channels is estimated in each coolant channel. By passing through each reactant channel, the reactants are then supplied to a membrane electrode assembly (MEA). Within the diffusion layer, the reactants diffuse to the catalyst layers, and the hydro- and dehydrogenation reactions occur at catalyst layers. Lastly, the polymer electrolyte membrane allows the protons moving to the other reaction site. It is assumed that the species diffusion, heat conduction and convection, and charge transport in the x-direction are negligible.

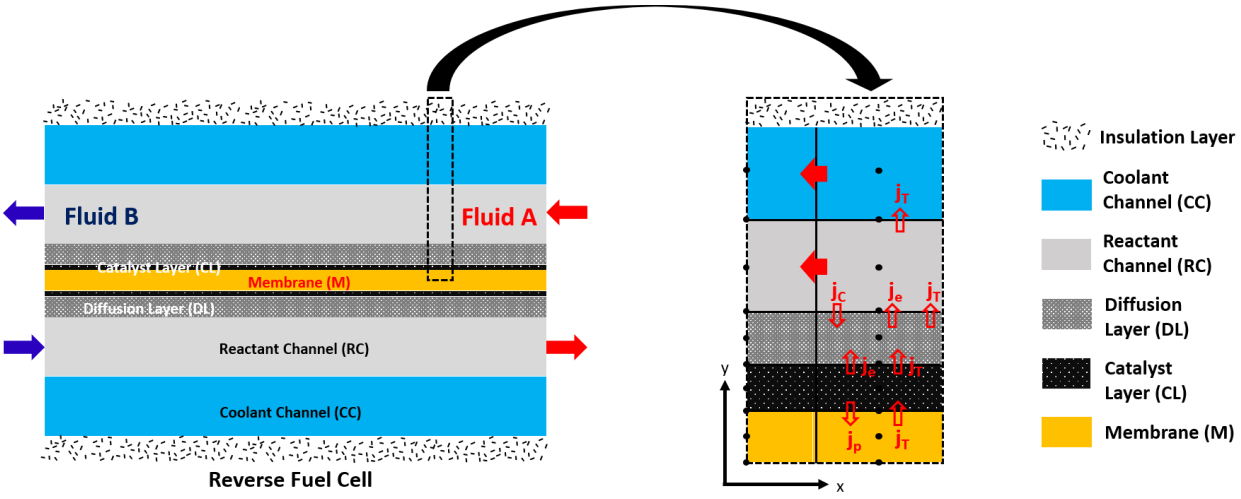

Figure 4: Schematic of the Reverse Fuel Cell

Table 1: Governing Equations (Kim et al., 2020)

Name	Domain	Equation	Reference
Ohm's Law for Electrons	RC-DL-CL	$j_e = -\sigma_e \nabla \varphi_e$	James, (2019); Vetter and Schumacher, (2019)
Ohm's Law for Protons	M	$j_p = -\sigma_p \nabla \varphi_p$	
Fourier's Law for Conduction	RC-DL-CL-M	$j_T = -k \nabla T$	
Newton's Law for Convection	CC	$j_T = h \Delta T$	
Fick's Law for Diffusion	DL	$j_C = -D \nabla C$	

2.3 Regenerator and Expansion Valve Modeling

After leaving the cell, the working fluid passes through a regenerator to make the system more efficient. By assuming a constant effectiveness and an adiabatic component, the regeneration effect can be expressed as Eq. (2):

$$q_{regen} = \varepsilon_{regen} \cdot \mathrm{Min}(h_2 - h_{2-b},\ h_4 - h_{4-b}) \tag{2}$$

where ε_{regen} is a constant regeneration effectiveness, and a minimum specific enthalpy difference is considered. The fluid then is throttled down to a low pressure through an expansion valve. It is assumed that the throttling process occurs isenthalpically as indicated in Eq. (3):

$$h_{2-b} = h_3 \tag{3}$$

2.4 Heat Exchanger and Line Set Modeling

A moving-boundary heat exchanger model is used to predict the performance of the evaporator. The two-phase and superheated vapor regions in the heat exchangers are determined by the moving-boundary algorithm. This algorithm combines an internal and an external pinching with a bounded solver for the model robustness, which allows the model to determine the temperature profile and the thermal load. The detailed methodology can be found in Bell et al. (2014). Along with the algorithm, both single- and two-phase heat transfer and pressure drop correlations have been implemented and are summarized in Table 2.

A line set model is employed to calculate the heat transfer rate, the pressure drops, and the working fluid charge between each cycle component. To estimate these output parameters, appropriate correlations have been employed depending on the phase of the thermodynamic states (refer to Figure 2) as indicated in Table 2: liquid (①, ②, ②-b, and ⑤), two-phase (③), and gas (④ and ④-b).

Table 2: List of Correlations used in a Heat Exchanger and a Line Set

Domain	Parameter	Correlations
Refrigerant-side	Single-phase pressure drop	Chruchill, (1977)
	Single-phase heat transfer	Gnielinski, (1976)
	Two-phase pressure drop	Lockhart-Martinelli, (1949)
	Two-phase evaporation heat transfer	Shah, (1976)
	Two-phase void fraction	Zivi, (1964)
Air-side	Heat transfer Pressure drop	Wang et al., (1998)

2.4 Charge Modeling

The working fluid charge is estimated by summing up the component charges including the reverse fuel cell, the evaporator heat exchanger, and line sets. For estimating the charge of the reverse fuel cell, the change of concentration is taken into consideration as indicated in Eq. (4),

$$m_{cell} = \int \rho_{mix} dV = \sum_i (c_{IPA,i}\rho_{IPA,i} + c_{ACTN,i}\rho_{ACTN,i})V_i \quad (4)$$

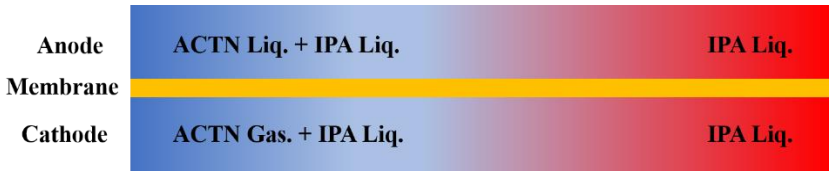

Figure 5: Schematic of Charge Distribution within the Cell

where $c_{species,i}$ is the mass fraction (concentration) and subscript *i* refers to the discretized segment. This method is used for calculating an isopropanol (IPA) and an acetone (ACTN) mixture density at both anode and cathode flow channels, respectively, shown in Figure 5. It is important to note that the gaseous ACTN density is used at the cathode and the degree of a conversion is crucial for determining the charge within the cell.

The evaporator and line sets share the correlations given in Table 2. The total charge can then be predicted by summing of the densities over all components, as expressed in Eq. (5), where *j* corresponds to each component (Shen et al., 2006). For simplicity, the amount of charge in a pump is not considered in this study.

$$m_{total} = \sum_j m_j \quad (5)$$

Table 3: Baseline Operating Conditions for Sensitivity Analysis

Component	Parameter	Value	Parameter	Value
System	Source temperature (°C)	26.7	Mass flow rate (mg/s)	0.02 ~ 2.0
	Sink temperature (°C)	35	Charge (g)	25~50,000
	Hydrogenated fluid (-)	Isopropanol	Pump efficiency (-)	0.8
	Dehydrogenated fluid (-)	Acetone	Regenerator efficiency (-)	0.6
Reverse Fuel Cell	Number of cells (-)	8	Thickness of each domain	James (2019)
	Area of unit cell (cm^2)	3~3,000	Membrane material properties	
	Coolant mass flow rate (mg/s)	500	Catalyst material properties	
	Channel width (m)	1e-4	Transport properties	
Heat Exchanger	Number of tubes per bank (-)	4	Horizontal spacing between banks (-)	0.02254
	Number of circuits (-)	5	Vertical spacing between bank (-)	0.03598
	Number of bank (-)	1	Fins per pinch	14.5
	Length of Tube (m)	0.10795	Fin height (m)	0.001
	Outer diameter (m)	0.009525	Fin pitch (m)	0.001
	Inner diameter (m)	0.0089154	Fin thickness (m)	0.00011
	Conductivity (W/m-K)	237	Relative humidity (-)	0.51
	Air flow rate (m^3/s)	0.049		
Line Sets	Length of tube (m)	0.2	Outer heat transfer coeff. (W/m^2-K)	1e-10
	Outer diameter of tube (m)	0.009525	Thickness of insulation (m)	0.02
	Inner diameter of tube (m)	0.007986	Conductivity of insulation (W/m-K)	0.036
	Conductivity of tube (W/m-K)	0.19		

3. RESULTS AND DISCUSSION

3.1 Model Evaluation

The main reason for developing the detailed system model is to investigate the effects of the working fluid charge levels on system performance, which can lead to a better understanding of system behavior and the accurate estimation of cycle performance.

For a baseline, source and sink temperatures were selected using the AHRI standard 210/240 (2017) A_{full} test conditions. Knowing that the model has been developed for a low capacity in a range of 0.01 mW to 1 W, similar to other reported values in the literature (McKay ets al., 2019; Poletayev et al., 2018), the mass flow rates and the charge of the system are given on a gram scale in this study. Isopropanol and acetone were used as the baseline working fluid pair due to their superior performance (James et al., 2019). In addition, 8 individual cells were utilized based on the results from the previous study (Kim et al., 2020; James, 2019). Lastly, given the fact that the flow rate is relatively small, the heat exchanger and the line set geometries were selected as indicated in Table 3.

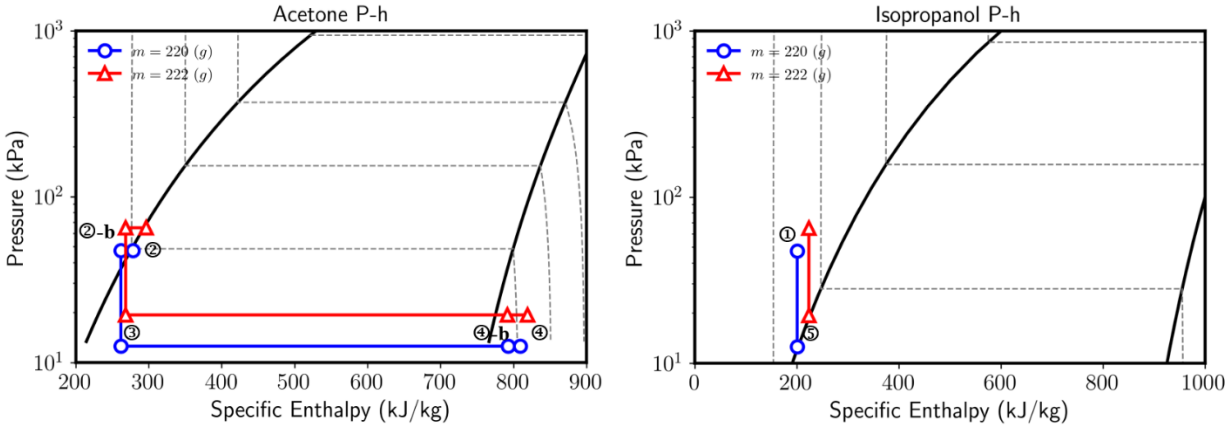

Figure 6: P-h Property Plots for Hydrogenated (Isopropanol) and Dehydrogenated (Acetone) Fluids

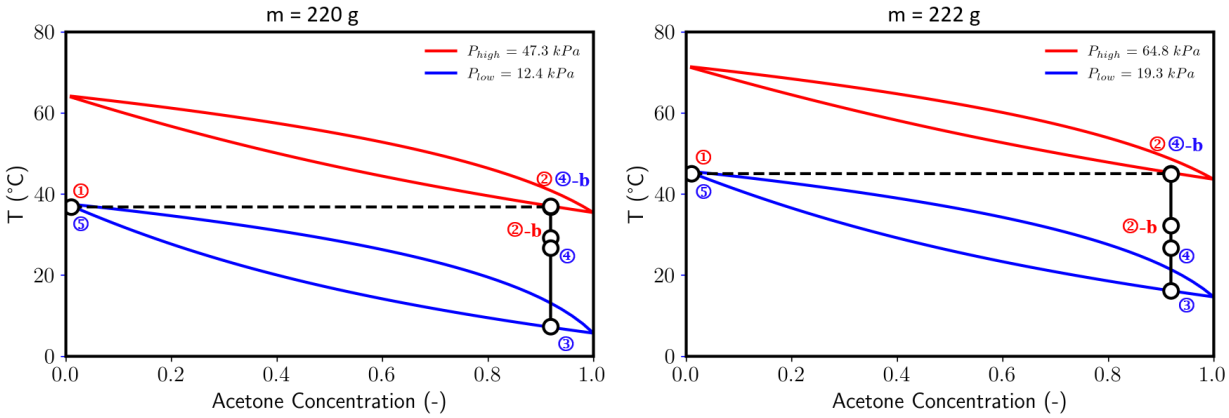

Figure 7: T-x Property Plots for Different Charge Inputs: m = 220 g (Left), m = 222 g (Right)

The first analysis evaluated the effect of two different charges on system state points for a cell area of 200 cm^2 and mass flow rate of 76 μg/s. As shown in Figure 7, it is clear that different charge levels lead to a change in the system properties, where the red and blue colors refer to the high and the low pressure sides of the system, respectively. The subcooled liquid at state ① converted into the high volatile fluid through the dash line. The processes between ② and ④-b in the vertical line are a heat absorbing processes identical to a vapor compression. The fluid then returns back to the less volatile fluid at saturated liquid state ⑤. If the system is overcharged, for example, the extent of a reaction in the cell (Δξ, which is x-axis in Figure 7) is reduced due to the charge calculation in Eq. (4). In other words, a mass fraction of a gaseous ACTN at the cathode is reduced as a result of a decrease in the degree of conversion. This lower conversion leads to an increase in the cell temperature for high ΔT between the cell and the ambient to maintain a certain amount of heat transfer. This is because the less amount of the more volatile ACTN at the outlet of the cell provides inefficient heat rejection from the cell. As a result of this, the system high pressure (P_{high}) and low pressure (P_{low}) increase with charge as shown in Figure 6. Once the system pressure is shifted to a high level, bubble and dew point temperatures are elevated accordingly as seen in Figure 7. The heat transfer of the evaporator (state ③ and ④) is then decreased by the shift of temperatures and thermal mass of the IPA liquid caused by incomplete conversion. Lastly, due to the high ΔT of regenerator inlets (state ② and ④), the amount of regeneration is increased.

3.2 Sensitivity Analysis

To understand the system behavior further, the influence of source and sink temperatures on performance are also investigated. To run the simulations, the two independent variables T_{cell} and $\Delta\xi$ have been kept constant. As shown in Figure 8(a), as the source temperature rises, the COP_c dramatically increases in the range of 17 °C to 25 °C and then gradually reaches a saturation point. This behavior is attributed to a transition from fully latent heat transfer to increased sensible heat of the working fluid in the evaporator after 25 °C. Similarly, the portion for latent heating decreases as the sink temperature rises due to increase in quality at the state ③ in the bottom left corner plot. As a result, the evaporator heat transfer rate does not increase as quickly as the power input leading to reduced COP_c.

In addition, the COP_c decrease with decreasing sink temperature in Figure 8(b). To explain this, let us now consider important characteristics of electrochemical devices that the amount of power generated or required during reactions is affected by the cell temperature. If you think about isothermal electrochemical cells, the coulombic work is estimated by the change in specific Gibbs Free Energy (Δg), where the Δg calculated by the change in specific enthalpy (Δh) and the change in specific entropy multiplied by temperature (TΔs) in Eq. (7):

$$\Delta g = \Delta h - T\Delta s \tag{7}$$

In the model, the cell temperature is linked to $T_{sink,}$, which means a decrease in T_{sink} leads to a reduced cell temperature. Moreover, according to Eq. (7), the term (TΔs) also decreases; thus, the required columbic work input (which is Δg) for driving the target reaction increases. As a result, the COP_c is reduced despite of the greater amount of latent in the range of low T_{sink} conditions.

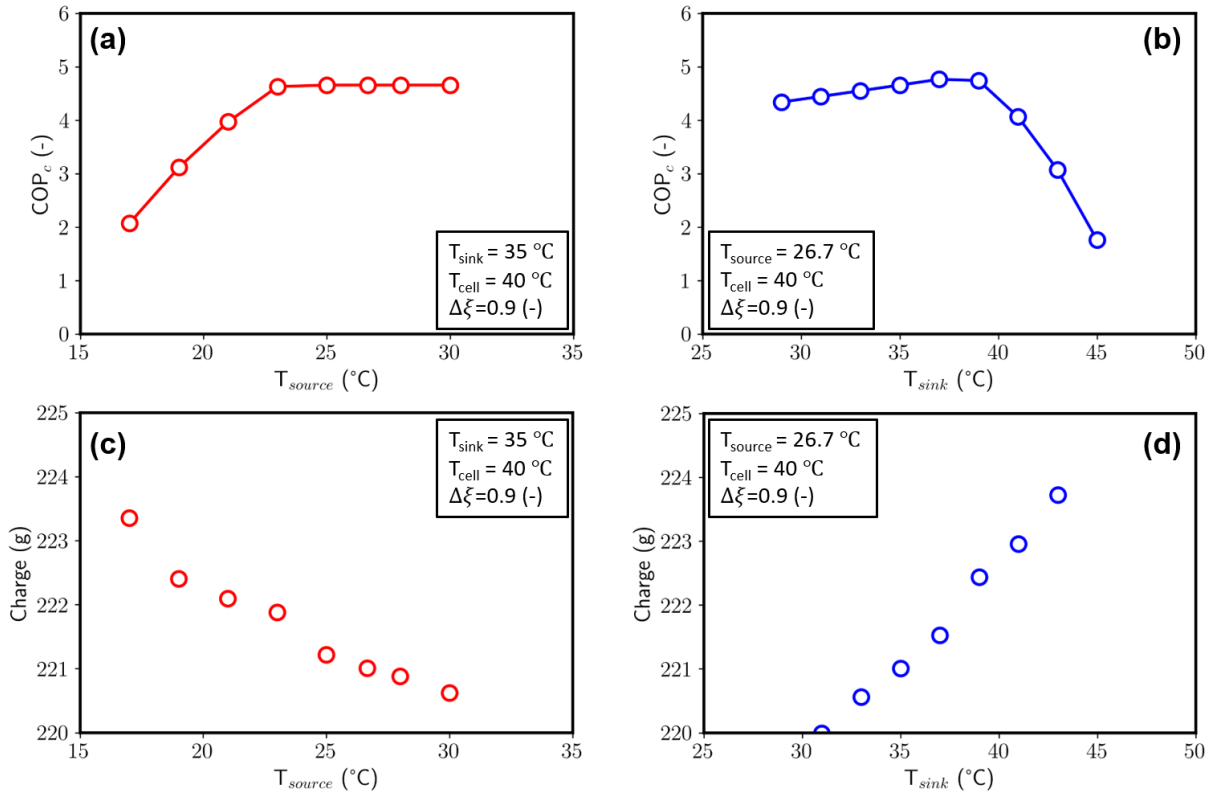

Figure 8: Effect of source and sink temperatures on system COP and charge.

Lastly, there is a different charge level at a given operating condition, which affects the system COP_c. For instance, in Figure 8(c), if the T_{source} increases up to 30 °C, the system COP_c is estimated to be 4.7 (-) in Figure 8(a) at a charge of 220.5 g. Similarly, if the T_{sink} goes down to 30 °C, the system COP_c is calculated as 4.2 (-) at a given charge of 220 g in Figure 8(b) and (d). As long as the system keeps the same operating conditions, the performance will be varied depending on the charge inputs.

The reason why an estimated system charge is affected by the system temperatures in this plot is attributed to the length of two-phase region in the evaporator. To be specific, high T_{source} lead to the fluid reaching the bubble point temperature faster than the low T_{source} in the evaporator, resulting in the small amount of charge, whereas the low T_{source} yield the large amount of charge. Unlike the T_{source} effects, T_{sink} which is coupled with the cell temperature (T_{cell}) affects the system charge differently based on changing system pressures. In this model, the system pressure is determined at the state ② and ⑤ using Eq. (8):

$$P = P_{sat}(T_{cell}, C_{fluids}) \tag{8}$$

where P_{sat} is saturation pressure and C_{fluids} is molar concentrations of fluids calculated from the degree of reaction ($\Delta\xi$). By definition, the system pressures rise as a result of increase in T_{sink}. This leads to the lower quality of evaporator inlet, thus having an increased charge amount due to a larger portion of a saturated liquid in the evaporator.

Using the improved model, the normalized performance map published by Kim et al. (2020) was updated as illustrated in Figure 9. The gray shaded region corresponds to the expected COP_c with respect to the cooling density with various mass flow rates, cell areas, and charges. The data were obtained based on the permutation of charge inputs, cell area, and mass flow rate for a given heat exchanger geometry. The data points indicate the different mass flow rates used, whereas charge was varied between 25 g and 50,000 g while single cell area varied between 3 cm^2 and 3000 cm^2, respectively. The cooling capacity, which is directly proportional to the mass flow rate, was normalized using a given cell area for this plot. It is worth noting that the required area of a cell for a target cooling capacity and COP_c can be estimated using this plot. This result would be employed to more accurately estimate the system performance and assess commercial viability in the future.

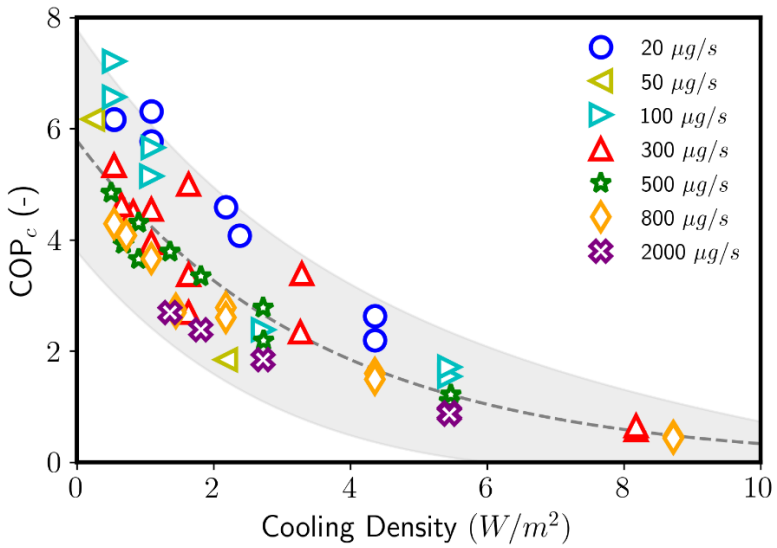

Figure 9: Re-evaluated Normalized Performance Map (Modified from Kim et al., 2020)

3.3 Model Limitations

Due to the formulation of this model, the following critical assumptions and constraints were required for model convergence. In the future, model validation and improvement will be performed based on comparisons of predictions with experiment results.

- For simplicity, the states ② and ⑤ in Figure 2 are set as saturated liquid states.
- For simplicity, the reverse fuel cell model is guaranteed to achieve a certain degree of reaction calculated from iterative processes. This means the model neglects an unexpected the extent of reaction, which could lead to fluid accumulation or depletion during cycling.
- At given geometries (cell and heat exchanger), there is a range of charges that could be applied to the model for convergence. If an unrealistic charge input is given, the model will not converge.

- Appropriate bounded values of two independent parameters (T_{cell} and $\Delta\xi$) for iterations is needed for a multivariable optimization described in the system modeling section. For example, the maximum T_{cell} can be goes up to 10 °C greater than T_{sink} (without using external heat source); the concentration change is set as greater than 0.75, meaning that certain amount of conversion (75 %) should be required for operating the cell model.
- The simulation time was nearly 30 min for each data point in Figure 9 due to the multivariable optimization process.

4. CONCLUSIONS

This paper focused on the development of a charge-sensitive mechanistic model based on a previously developed models that was combined with the ACHP open-source code. A bounded multivariable optimization scheme is utilized for the solution process. Two independent parameters – cell temperature and the extent of reaction – are iteratively determined until satisfying convergence criteria. Lastly, the paper re-evaluated the normalized performance curve published in Kim et al. (2020). This upgraded performance curve could be used for a more accurate estimation of system performance and future scalability assessments.

NOMENCLATURE

ACNT	acetone (-)	c	mass concentration (-)
C	molar concentration (mol/m^3)	CC	coolant channel (-)
CL	catalyst layer (-)	COP	coefficient of performance (-)
D	diffusivity (m^2/s)	DL	diffusion layer (-)
h	conv. heat transfer coeff. (W/m^2-K)	IPA	isopropanol (-)
j	flux (1/m^2-s)	k	thermal conductivity (W/m-K)
m	charge (g)	$\dot{m}$	mass flow rate (μg/s)
M	membrane (-)	Min	minimum (-)
P	pressure (kPa)	RC	reactant channel (-)
T	temperature (°C)	V	volume (m^3)
$\dot{W}$	power (W)	x	molar fraction (-)
ρ	density (kg/m^3)	ε	efficiency (-)
σ	electrical conductivity (S-m)	ξ	extent of reaction (-)
φ	potential (V)	υ	specific volume (m^3/kg)

Subscript

ACTN	acetone	c	cooling
C	molar concentration	cell	electrochemical cell
e	electron	high	high-side pressure
i	discretized segment	inf	infinity
j	component	low	low-side pressure
mix	mixture	p	proton
regen	regenerator	T	temperature

REFERENCES

AHRI Standard 210/240. (2017). Performance rating of unitary air-conditioning and air-source heat pump equipment

Bahman, A. M., Ziviani, D., & Groll, E. A. (2018). Development and validation of a mechanistic vapor-compression cycle model. *International Refrigeration and Air Conditioning Conference.* West Lafayette, Purdue University. https://docs.lib.purdue.edu/iracc/1968

Bell, I. H., Quoilin, S., Georges, E., Braun, J. E., Groll, E. A., Horton, W. T., Lemort, V. (2014). A generalized moving-boundary algorithm to predict the heat transfer rate of counterflow heat exchangers for any phase configuration. *Applied Thermal Engineering, 79(25)*, 192-201

Bell, I. H. (2015). Air conditioning and heat pump model (ACHP) source code version 1.5. [Online; accessed 10-April 2018]. https://github.com/CenterHighPerformanceBuildingsPurdue/ACHP

Battelle Memorial Institute. (2016). Manufacturing cost analysis of 100 and 250 kW fuel cell systems for primary power and combined heat and power applications.

Broyden, C. G. (1965). A class of methods for solving nonlinear simultaneous equations. *Mathematics of computation, 19(92)*, 577-593. http://www.jstor.org/stable/2003941

Churchill, S. W. (1977). Friction-factor equation spans all fluid-flow regimes. *Chemical Engineering, 84(24)*, 91-92

European Commission. (2016, December). EU phasedown on track as fluorinated greenhouse gas use falls, *European Commission.* https://ec.europa.eu/clima/news/articles/news_2016121301_en

Fil, B. E., Boman, D. B., Tambasco, M. J., Garimella, S. (2021). A comparative assessment of space-conditioning technologies. *Applied Thermal Engineering, 182*, 116-105.

Gnielinski, V. (1976). New equations for heat and mass-transfer in turbulent pipe and channel flow. *International Chemical Engineering, 16(2)*, 359-368.

Goetzler, W, Guernsey, M., Young, J., Fuhrman, J., & Abdelaziz, O. (2016). The future of air conditioning for buildings. *Department of Energy Office of Energy Efficiency and Renewable Energy Building Technologies Office, July*, 94. www.osti.gov/home/

Goetzler, William, Zogg, R., Young, J., & Johnson, C. (2014). Alternatives to vapor-compression HVAC technology. *ASHRAE Journal*, *56*(10), 12–23.

James, N. A. (2019). *Investigation of chemical looping for high efficiency heat pumping* (PhD Thesis). Purdue University, West Lafayette

James, N. A., Braun, J. E., & Groll, E. A. (2019). The chemical looping heat pump: Thermodynamic modeling. *International Journal of Refrigeration*, *98*, 302–310. https://doi.org/10.1016/j.ijrefrig.2018.11.005

Kim, J., James, N. A., Groll, E. A., Braun, J. E., Ziviani, D. (2020). Scalability of chemical looping heat pump technology. *2100*(July). https://doi.org/10.18462/iir.rankine.2020.1200

Lockhart, R. and Martinelli, R. (1949). Proposed correlation of data for isothermal two-phase, two-component flow in pipes. *Chemical Engineering Progress, 45(1)*, 39-48

McKay, I. S., Kunz, L. Y., & Majumdar, A. (2019). Electrochemical redox refrigeration. *Scientific Reports*, *9*(1), 1–8. https://doi.org/10.1038/s41598-019-50118-y

Poletayev, A. D., McKay, I. S., Chueh, W. C., & Majumdar, A. (2018). Continuous electrochemical heat engines. *Energy and Environmental Science*, *11*(10), 2964–2971. https://doi.org/10.1039/c8ee01137k

Powell, M. (1964). An efficient method for finding the minimum of a function of several variables without calculating derivatives, *The Computer Journal, 7(2)*, 155-162. https://doi.org/10.1093/comjnl/7.2.155

Shah, M. M. (1976). A new correlation for heat transfer during boiling flow through pipes. *ASHRAE Transactions, 82*, 66-86

Shah, M. M. (1979). A general correlation for heat transfer during film condensation inside pipes. *International Journal of Heat and Mass Transfer, 22(4)*, 547-556

Shen, B., Braun, J. E., Groll, E. A. (2006). Some Modeling Improvements for Unitary Air Conditioners and Heat Pumps at Off-Design Conditions. *International Refrigeration and Air Conditioning Conference.* West Lafayette, Purdue University.

U.S. Department of Energy. (2016). The road to zero: DOE's next-generation heating and cooling R&D strategy. *Department of Energy Office of Energy Efficiency and Renewable Energy Building Technologies Office.* https://www.energy.gov/eere/buildings/road-zero-does-next-generation-heating-and-cooling-rd-strategy

U.S. Energy Information Agency. (2019). Annual Energy Outlook 2019 with projections to 2050. *Annual Energy Outlook 2019 with Projections to 2050*, *44*(8), 1–64. https://www.eia.gov/outlooks/aeo/pdf/aeo2019.pdf

Vetter, R., & Schumacher, J. O. (2019). Free open reference implementation of a two-phase PEM fuel cell model. *Computer Physics Communications*, *234*, 223–234. https://doi.org/10.1016/j.cpc.2018.07.023

Wang, C., Tsai, Y., Lu, D. (1998). Comprehensive study of convex-louver and wavy fin-and-tube heat exchangers. *Journal of Thermophysics and Heat Transfer, 12(3)*. https://doi.org/10.2514/2.6354

Ziviani, D., Woodland, B. J., Georges, E., Groll, E. A., Braun, J. E., Horton, W. T., Van Den Broek, M., & De Paepe, M. (2016). Development and a validation of a charge sensitive organic Rankine cycle (ORC) simulation tool. *Energies*, *9*(6). https://doi.org/10.3390/en9060389

Zivi, S. M. (1964). Estimation of steady-state steam void-fraction by means of the principle of minimum entropy production. *Journal of Heat Transfer, 86(2)*, 247-251

ACKNOWLEDGEMENT

The authors gratefully acknowledge the support from the Center for High Performance Buildings (CHPB) at the Ray W. Herrick Laboratories, Purdue University.